Journal of Materials Chemistry A

Accepted Manuscript

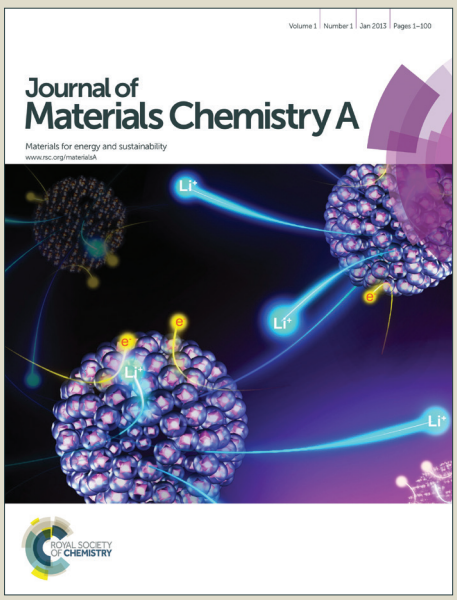

ROYAL SOCIETY OF CHEMISTRY

www.rsc.org/materialsA

Hierarchical $Cu_{0.27}Co_{2.73}O_4/MnO_2$ nanorod arrays grown on 3D nickel foam as promising electrode materials for electrochemical capacitors

Hongwei Ge, Chengxiang Wang, Longwei Yin*

Key Laboratory for Liquid-Solid Structural Evolution and Processing of Materials, Ministry of Education, School of Materials Science and Engineering, Shandong University, Jinan 250061, P. R. China

Email: yinlw@sdu.edu.cn

Abstract

$Cu_{0.27}Co_{2.73}O_4/MnO_2$ hybrid hierarchical nanostructure arrays directly on pressed nickel foam, with thin MnO_2 nanoflakes homogeneously wrapped on $Cu_{0.27}Co_{2.73}O_4$ nanorod arrays, are successfully synthesized by a simple hydrothermal and post heat-treatment method. The microstructures, phase structure, crystalline state, chemical component and chemical bonding state of the hybrids are systematically characterized using XRD, XPS, SEM and TEM, respectively. The electrochemical performance of the $Cu_{0.27}Co_{2.73}O_4/MnO_2$ hybrid electrode for electrochemical capacitors (EC) is investigated using cyclic voltammetry (CV), galvanostatic charge-discharge and electrochemical impedance spectroscopy (EIS) techniques. A superior areal capacitance of ~4 Fcm^{-2} can be obtained for $Cu_{0.27}Co_{2.73}O_4/MnO_2$ hybrid electrode even at higher current density of ~18.6 $mAcm^{-2}$. the 3D $Cu_{0.27}Co_{2.73}O_4/MnO_2$ hierarchically porous nanorod array structures endow the electrodes with large specific surface area and improve path way for ion diffusion, thus leading to high areal capacitance and excellent rate capability, and indicate their promising application as binder-free electrodes for high performance EC and potentiality triggering the exploration for improved areal capacitance for miniaturized devices.

1. Introduction

Energy storage, as a key component in energy conversion-storage-delivery chain, depends heavily on the development of electrical energy storage (EES) systems.[1-3] An important type of EES devices is electrochemical capacitor (EC) or pseudocapacitor, which is recognized by Conway and other scientific researchers in the 1970s.[4] Unlike traditional batteries, EC can deliver hundreds of or even thousands of times larger than similar-sized batteries in power density. In addition, the highly reversible redox reactions in EC do not induce the volume changes as usually happened in the charge-discharge processes of the battery, resulting in a longer cycle life for EC than the traditional battery.[5, 6] What's more, EC has advantages over batteries in applications requiring a high spike of current where probably generating an intense polarization as a result of the slow lithium diffusion in the active material and the increased resistance of the electrolyte at high charge-discharge rate.[2, 7]

Among electrode materials, metal oxides possess abundantly changeable valence state, and particularly those with novel architectures provide multiple accessible electroactive sites, appearing quite suitable for the application of ECs.[8] Such consideration also relies on the fact that metal oxides can not only deliver 10-100 times higher energy density than carbon-based electrical double layer capacitors, but also maintain better structural integrality than polymer-materials-based ECs. It is well known that the performance of ECs depends heavily on the electrochemical activity and kinetics of the electrodes. The electrochemical activity of the electrodes is mostly relied on electroactive sites, and the reaction kinetic of the electrode materials is mainly determined by the ion diffusion ability and electronic conductivity during the energy storage processes.[9-11] Therefore, due to the intrinsic poor electrical conductivity of metal oxides, the performances such as specific capacitance, rate capability and cycle performance, etc., remain undesirable. Additionally, because the redoxbale reaction for ECs only occurs in a limited region near the surface,[12-14] the bulk materials cannot be utilized sufficiently without contribution to the capacity.

Much efforts have been paid to address these problems. For example, Hu *et al.* prepared the nickel cobaltite aerogels as electrode materials for ECs, showing extremely high capacitance of 1400 F g^{-1} at 25mV s^{-1} with a mass loading ~0.4 $mgcm^{-2}$ (within a potential window of 0.04-0.52V, 1M NaOH as the electrolyte),[7] closely to the highest value of 1580 Fg^{-1} earlier reported for hydrous ruthenium oxides ($RuO_2 \bullet nH_2O$) by themselves.[15] However, it is noted that the mass loading is relatively low, only ~0.4 mg cm^{-2}, which should partially be responsible for the high capacity. Actually, in most cases,[7, 16, 17] as the mass loading increases, the performance may not scale up simultaneously since the interior 'dead volume' is unavailable.

3D nanostructure array architecture can offer not only large specific surface area, but also the improved path for ions diffusion and electron transportation. Further depositing metal oxide on such 3D conductive skeleton to form a hierarchical nanostructure can make a more fully utilization of the space, which has been demonstrated to be the promising electrode materials for high performance ECs.[9, 18] Recently Fan and colleagues proposed that oriented hierarchical core-shell architectures can make use of the advantages of both components to enhance the utilization of the active materials.[19-22] The novel design that composed of pseudocapacitive metal oxides directly grown on 3D conductive substrates made use of the coordinative contribution of each component to ensure the fast ion and electron transfer, resulting in an excellent performance. The similar strategy to enhance the capacitor performance has been adopted by other researchers, e.g. Lou,[9, 13, 23] Sun,[14,18,24] Shen,[25, 26] further confirming its effectiveness.

Nowadays, the ever-increasing miniaturization trend of electronic devices requires the power supply units should have smaller dimension than before, while maintaining high enough energy supply. Correspondingly, as for ECs, meeting these demands needs the combination of high mass loading and high utilization of the electrode materials, i.e., a high areal capacity. Though the specific capacitance of pseudocapacitive material mentioned above[9, 19-22] were higher than those synthesized by traditional slurry-coating-technique that was commonly polymer binder involved methods, they are hardly to say to exhibit practically desirable electrochemical performance because their mass loading was relative low. For example, Co_3O_4@MnO_2 core-shell arrays show a specific capacitance of ~480 F g^{-1} at ~2.67 A g^{-1}, however, the corresponding areal capacitance (C_a) was only 0.72 F cm^{-2} caused by a low mass loading of Co_3O_4: ~0.8 mg cm^{-2}, MnO_2: ~0.7 mg cm^{-2}.[19] C_a of Co_3O_4@NiO core-shell arrays can retain 2.56 Fcm^{-2} after 6000 cycles with a coulombic efficiency ~95.1% at 2A/g (mass loading Co_3O_4: ~2.1 mgcm^{-2}, NiO: ~0.9 mgcm^{-2}),[22] Both the Co_3O_4@MnO_2 and Co_3O_4@NiO composites show lower performance than the $Cu_{0.27}Co_{2.73}O_4$/MnO_2 composite. Similar phenomena were also observed in many other related works.[3, 9, 20-22] In this regard, increasing the mass loading of active materials to achieve high areal capacitance would be better than only pursuing high specific capacitance for the practical application of miniaturized energy storage device.

Though Co_3O_4 electrodes as electrodes for electrochemical capacitor display relatively high capacitance, considerable phys-chemical and large volume and strain change during the long-term cycling may result in poor cycling performance. Furthermore, low electrical conductivity and poor structural stability make the rate capability and capacitance retention of Co_3O_4 electrodes far from satisfactory.[1, 2] The ultrathin MnO_2 nanoflakes outside $Cu_{0.27}Co_{2.73}O_4$ guarantee the fast ion and electron transportation, the effective ion penetration into the core region, thus both of core and shell can react with anions and cations in electrolyte, enhancing the utilization of active materials. Most importantly, MnO_2 can serve as a protective layer to maintain the structural integrity during long-term redox chemical reaction.

According to aforementioned statements, the 3D hierarchical nanostructure incorporated pseudocapacitive and conductive components are promising to produce a high areal capacity to meet the demands for miniaturization of energy storage devices. In this work, copper cobalt oxide nanorod arrays, showing both conductive and pseudocapacitive, are successfully synthesized by a simple hydrothermal method, and then covered with MnO_2 nanoflakes through hydrothermal deposition process. The composite electrodes possess high mass loading up to ~4.4 mg cm^{-2} and ~6.2 mg cm^{-2} for $Cu_{0.27}Co_{2.73}O_4$ and $Cu_{0.27}Co_{2.73}O_4$/MnO_2, respectively, exhibiting high areal capacitance of ~2 and 4 F cm^{-2} at 8.8 mAcm^{-2} for $Cu_{0.27}Co_{2.73}O_4$ and 18.6 mAcm^{-2} for $Cu_{0.27}Co_{2.73}O_4$/MnO_2, much better than that of $CuCo_2O_4$ related materials recently reported.[27, 28] $Cu_{0.27}Co_{2.73}O_4$ and $Cu_{0.27}Co_{2.73}O_4$/MnO_2 can offer better rate capability, higher capacity, lower electrochemical impedance, etc. than those of $CuCo_2O_4$.[27] By comparing with mesoporous $CuCo_2O_4$ nanograss grown on copper foam (~4mgcm^{-2}),[28] $Cu_{0.27}Co_{2.73}O_4$ and $Cu_{0.27}Co_{2.73}O_4$/MnO_2 exhibit lower electrochemical impedance and the rival capacitance, capacitance retention and long-term cycling properties, even though possessing higher active material loading. $Cu_{0.27}Co_{2.73}O_4$/MnO_2 hybrids are expected to trigger the exploration for improved areal capacitance.

2. Experiment section

2.1 Fabrication of $Cu_{0.27}Co_{2.73}O_4$/MnO_2 nanorod arrays on pressed nickel foam

All chemicals used are of analytical grade. Nickel foams usually act as substrates of the electrode for ECs, particularly when fabricating high loading electrodes, due to their high electron conductivity, novel 3D architectures and hydrophilicity.[18, 29] It is wise to substitute them with the pressed ones that not only maintains the novel 3D architectures, but also decrease their thickness and quality.

First of all, a piece of nickel foam (pressed under 20 MPa by sheeting presser, ~3×5 cm^2, ~32.5 mg cm^{-2}) was degreased with acetone for 20 min, then etched with 6.0 mol L^{-1} HCl for 20 min, finally rinsed with ethanol and water for 20 min with the assistance of ultrasonication, respectively.[26, 30] Then, a piece of dried substrate was immersed into the homogeneous solution mixing with 0.5 mmol of $Cu(NO_3)_2 \cdot 3H_2O$, 5 mmol of $Co(NO_3)_2 \cdot 6H_2O$, 10 mmol of NH_4F, 25 mmol of $CO(NH_2)_2$ and 50 mL of ultrapure water that contained in Teflon-lined stainless steel autoclaves. The autoclave was sealed and maintained at 120℃ for 5 h, then cooled down to room temperature spontaneously. Finally, the substrate was collected, rinsed with ultra pure water several times and dried at 60℃. In this synthesis process, the main chemical reactions can be illustrated as the following equations.[31] Finally, the obtained samples were heated up to 400 ℃in air with a ramping rate of 3℃ min^{-1} and kept for 4 h to form $Cu_{0.27}Co_{2.73}O_4$ nanorods array.

$$Co^{2+} + Cu^{2+} + xF^- \leftrightarrow (Cu,Co)F_x \quad (1)$$

$$H_2NCONH_2 + H_2O \leftrightarrow 2NH_3 + CO_2 \quad (2)$$

$$CO_2 + H_2O \leftrightarrow CO_3^{2-} + 2H^+ \quad (3)$$

$$NH_3 \bullet H_2O \leftrightarrow NH_4^+ + OH^- \quad (4)$$

$$(Cu,Co)F_x + CO_3^{2+} + OH^- + nH_2O \leftrightarrow (Cu,Co)CO_3(OH)_2 \bullet nH_2O + xF^- \quad (5)$$

In order to prepare the ultrathin MnO_2 nanoflakes to cover the $Cu_{0.27}Co_{2.73}O_4$ nanorods, we adopted the carbon modified method.[19] Firstly, the substrate covered with the nanorod arrays was soaked into glucose aqueous solution (0.04 M) for 24h, then taken out and heated to 450 ℃ with a ramping rate of 3℃ min^{-1} in Ar gas for 2 h for carbonization. Sequentially, the carbon modified $Cu_{0.27}Co_{2.73}O_4$ nanorod arrays were transferred into 0.03M $KMnO_4$ solution in a Teflon-lined stainless steel autoclave, and maintained at 160℃ for 5 h. Finally, the substrate was collected and rinsed with ultra pure water several times with a following-up drying process at 60℃ to obtain a $Cu_{0.27}Co_{2.73}O_4/MnO_2$ hybrid array. The fabrication processes in section **2.1** and **2.2** are schematically illustrated in **Fig. 1**.

2.2 Structure characterization

The crystal structure of the as-synthesized materials is collected from Rigaku D/Max-KA X-ray diffractometer with Cu Kα radiation. SU-70 field emission scanning electron microscopy (FESEM) equipped with energy dispersive X-ray spectrometer (EDS) was employed to analyze the morphology and element distribution of the as-prepared samples. The microstructure of the synthesized products was analyzed using high-resolution transmission electron microscopy (HR-TEM) of JEM-2100 at an acceleration voltage of 200 kV. X-ray

photoelectron spectroscopy (XPS) of ESCALAB 250 with 150 W Al Kα probe beam was used to characterize the chemical composition and the oxidation state information.

2.3 Electrochemical Characterization

Electrochemical measurements were performed on an electrochemical workstation (PARSTAT 2273) using a three-electrode mode in 6 M KOH aqueous solution, with $Cu_{0.27}Co_{2.73}O_4/MnO_2$ hybrid arrays or pristine $Cu_{0.27}Co_{2.73}O_4$ nanorod arrays on pressed nickel foam as work electrode directly, Pt plate as counter electrode and Hg/HgO as reference electrode. The effective geometrical area for both work electrodes was ~1×1 cm^2, and mass loading were ~4.4 $mgcm^{-2}$ and ~6.2 $mgcm^{-2}$ for $Cu_{0.27}Co_{2.73}O_4$, $Cu_{0.27}Co_{2.73}O_4/MnO_2$, respectively. The difference of both values, ~1.8 mg cm^{-2}, was attributed to the mass of MnO_2. The quality of active materials was obtained by precision balance under the same condition. Cyclic voltammetry (CV) test was performed from 0 to 0.7 V with different scan rates. Galvanostatic cycled test was carried out on a LAND CT2001A instrument (Wuhan, china). The electrochemical impedance spectroscopy (EIS) measurement was performed by applying an AC voltage with a perturbation amplitude of 10 mV versus the open circuit potential in a frequency range from 0.01 Hz to100 kHz. Areal and specific capacitances were calculated using Equation (6) and (7), respectively, according to the discharge curves, where I is the constant discharge current, t is the discharging time, V is the voltage drop upon discharging, m is the total mass of the electrode material, and S is the effective geometrical area of the electrode.

$$C_a = \frac{I \times t}{\Delta V \times S} \quad (6)$$

$$C_{sp} = \frac{I \times t}{\Delta V \times m} \quad (7)$$

3. Results and Discussion

X-ray diffraction (XRD) measurement is carried out to determine the phase structure of the as-synthesized materials, as shown in **Fig. 2**. Three diffraction peaks at ~44.2, 51.8 and 76 degrees are indexed to (111), (200) and (220) planes of the nickel substrate (JCPDS Card No.65-0380).[9, 32] Apart from those of nickel substrate, the left peaks can be readily indexed to $Cu_{0.27}Co_{2.73}O_4$ (as the red line shown, JCPDS Card No.78-2173, face center cubic (fcc): 8.09Å×8.09Å×8.09Å <90º×90º×90º>, space group: $Fd\bar{3}m$), and MnO_2 (JCPDS Card No. 39-0375) as the pink line shown. No other characteristic peaks from impurities are detectable in the spectrum.

More detailed information of the elemental composition and the oxidation state of the as-prepared materials was revealed by XPS spctra. **Fig. 3**a displays the full scan spectra of $Cu_{0.27}Co_{2.73}O_4$, from which five elements can be resolved, C 1s (as reference), O 1s, Cu 2p, Co 2p, Ni 2p (come from nickel foam substrate). The peaks at 933.9 and 934.8 eV can be attributed to Cu $2p_{3/2}$ level, which is similar to that reported in CuO sample.[38] It is shown that Cu is incorporated into lattice of Co_3O_4 in the form of bivalence (Cu^{2+}). Sat.1 and sat.2 peaks indicate the presence of paramagnetic Cu^{2+}.[33] As previous study reveals, the main peak of Ni $2P_{3/2}$ is accompanied by a satellite peak with a larger binding energy than that of the main peak.[24] The XPS spectrum of Co 2p is well fitted to two spin-orbit doublets and three shakeup satellite peaks (sat.1, sat.2, sat.3), as shown in **Fig. 3**c.[23, 34] The peaks at 779.6 and 794.8 eV can be attributed to Co $2p_{3/2}$ and Co $2p_{1/2}$ level, corresponding to that of Co^{3+}, which is believed to be originated from characteristic spin-orbit doublets with a splitting range of ~15.2 eV, while those peaks at 780.9 and 796.4 eV correspond well with the tetrahedral Co^{2+}, with a Co $2p_{3/2}$-$2p_{1/2}$ characteristic

spin-orbit doublets with a splitting range of 15.5eV.[33, 34] The sat.1, sat.2, sat.3 peaks indicate the presence of paramagnetic Co^{2+}, Co^{3+}, respectively. The high-resolution spectrum for O 1s in **Fig. 3**d is deconvoluted into three peaks, the first one at 529.6 eV is characteristic of metal-oxygen bonds corresponding to Co-O and Cu-O.[11, 34, 35] The second one at 531.3 eV is typical of oxygen in an OH^- group.[18] The last one (at 534eV) is usually associated with the physically-and chemically-bonded water on the surface.[18] Additionally, the atomic ratio of Co to Cu elements is 18.6:1.9≈9.8, close to that of the precursor (5 mmol of $Co(NO_3)_2$•$6H_2O$, 0.5 mmol of $Cu(NO_3)_2$•$3H_2O$) and the results of XRD ($Cu_{0.27}Co_{2.73}O_4$ 2.73:0.27≈10).

Fig. 4 shows the different magnification SEM images of the novel 3D architectures of $Cu_{0.27}Co_{2.73}O_4$ nanorod arrays grown on the Ni foam. The texture of Ni foam seems unchanged in comparing **Fig. 4**a-**4**b with **Fig. S1**. More importantly, the 3D Ni substrate is uniformly covered with the nanorod arrays of ~150-200 nm, showing a homogeneously aligned structure (**Fig. 4**c-**4**d). Unlike the intertwined nanowires and nanowire bundles, the nanorods here appear independent, forming perpendicularly standing nanoarrays that is benefit for controlling the aggregation of the active materials and improving the path way for ion-diffusion and electron-transportation. Furthermore, the rough surface of each rod ascribed to the emission of the H_2O and gases during the annealing process can help to facilitate the penetration of the electrolyte and the utilization of active materials, leading to low charge transfer resistance and high capacitance of the electrode. The element distribution of $Cu_{0.27}Co_{2.73}O_4$ was further determined by energy eispersive x-ray spectrometry (EDX) mapping analysis (**Fig. S2**). The elemental mapping images show the existence of Cu, Co, O, Ni, which is in accordance with the XRD, XPS measurement.

Fig. 5a-**5**b depicts low FESEM images of $Cu_{0.27}Co_{2.73}O_4/MnO_2$ hybrids, similar to that of $Cu_{0.27}Co_{2.73}O_4$ nanorod arrays in **Fig. 4**a-**4**b. The magnified FESEM images in **Fig. 5**c-**5**d show different morphologies from that of pure $Cu_{0.27}Co_{2.73}O_4$ nanorod arrays. The MnO_2 nanoflakes are homogenously grown on $Cu_{0.27}Co_{2.73}O_4$, the surface of the nanorods gets rougher, and the diameter of the nanorods becomes larger. The average diameter of the hybrid nanorods after the growth of MnO_2 is ~250-300 nm. The characteristic structure of well arranged nanorod arrays is still remained. The inter-space between $Cu_{0.27}Co_{2.73}O_4$ rods and the adjacent MnO_2 nanoflakes is benefit for the effective penetration of the electrolyte, the utilization of active materials, reduction of the charge transfer resistance and high capacitance of the electrode. The outer layer that consists of hierarchically nanoporous MnO_2 nanoflake architecture does not hinder the effective electrolyte penetration into the inner $Cu_{0.27}Co_{2.73}O_4$ rods. The elemental mapping images of $Cu_{0.27}Co_{2.73}O_4/MnO_2$ show the existence of Cu, Co, O, Mn, Ni and their homogenous distribution along the whole sample. (**Fig. 6**)

The morphology and microstructure of $Cu_{0.27}Co_{2.73}O_4/MnO_2$ and $Cu_{0.27}Co_{2.73}O_4$ are further characterized by transmission electron microscopy (TEM). The TEM images of $Cu_{0.27}Co_{2.73}O_4$ in **Fig. 7**a-**7**b show that the seemingly continuous nanorods are actually composed of numerous densely-packed particles displaying a uniformly distribution in shape and size. The uniquely hierarchical structure with inter-particle mesopores can effectively facilitate electrolyte penetration and Li-ion diffusion.

The crystal structure of the as-prepared sample can be determined by the selected area diffraction pattern (SAED) shown in **Fig. 7**c. The SAED diffraction pattern tends to exhibit a typical polycrystalline pattern for the $Cu_{0.27}Co_{2.73}O_4$ nanorod, further confirming the nanorod sample is composed of nanoparticles with different particle orientations. The structural information obtained from SAED pattern agreed well with those from XRD analysis. The HRTEM lattice image of $Cu_{0.27}Co_{2.73}O_4$ in **Fig. 7**d is taken from the gray-box area in **Fig. 7**b. The

particle acting as building blocks of the nanorods exhibits a perfect single-crystalline structure with a clear 2-D lattice fringe. There are two sets of distinct inter-planar spacing of ~ 0.29 nm and ~0.24 nm, corresponding to that of $(\bar{1}\bar{3}1)$ and $(0\bar{2}2)$planes of $Cu_{0.27}Co_{2.73}O_4$, respectively. The insert is the corresponding Fourier transformation pattern of the lattice image.

TEM image of $Cu_{0.27}Co_{2.73}O_4/MnO_2$ (**Fig. 8**a) unambiguously reveals that the $Cu_{0.27}Co_{2.73}O_4$ nanorods are homogeneously entirely and intimately coated with flaky MnO_2, which would be helpful to increase the energy and power output per area. Though the $Cu_{0.27}Co_{2.73}O_4$ nanorods are covered with ultrathin MnO_2 nanoflakes, the uniformity of nanorod structure is still well retained. The structure of the $Cu_{0.27}Co_{2.73}O_4/MnO_2$ sample is determined by the SAED pattern in **Fig. 7**b. The ring markings with gray-color are in good agreement with that of (210), (202), (212), (511) of MnO_2, while the others correspond with that of (220), (311), (400), (422), (440), (622) planes of $Cu_{0.27}Co_{2.73}O_4$. **Fig. 8**c-**8**d gives a typical TEM images of MnO_2 nanoflakes, showing layered structures interconnected with each other to form a highly porous morphology. The bending, curling, crumpling of the dark strips areas were attributed to the folding ultrathin MnO_2 layers. The lateral size of the MnO_2 nanoflakes is ~50 nm, and the thickness is ~3-4 nm, consisting of ~6-7 layers that can be clearly determined from the numbers of the curling folded edges. Thus, nearly all the core-shell nanorod arrays are easily accessible to electrolytes for energy storage *via* the convenient diffusion channels.

To explore the potential applications of the as-prepared samples, the $Cu_{0.27}Co_{2.73}O_4$ and $Cu_{0.27}Co_{2.73}O_4/MnO_2$ electrodes are fabricated for ECs. The electrochemical performance is evaluated via cycle voltammogram (CV) and galvanostatic charge-discharge (GCD), and electrochemical impedance spectra (EIS) measurement. The CV measurement for $Cu_{0.27}Co_{2.73}O_4$ is conducted at different scan rates from 5 to 100 mVs^{-1} (**Fig. 9**a). The shape of the CV curves obviously reveals a pseudocapacitive behavior. A pair of expanded redox peaks is observed and all profiles exhibits the similar shapes. As the scan rate increases, the current density and integral area of the CV curves increase, and the separation of potential peaks owing to polarization and ohmic resistance take place gradually. Even at 100 mVs^{-1}, the shape of the CV curve remains almost unchanged, indicating fast redox reaction on the surface. More importantly, undramatic peak potential shifts during this process suggests its characteristic of lower polarization and resistance, and high rate capability.[23] The expanded peaks of $Cu_{0.27}Co_{2.73}O_4$ in CV curves are mainly attributed to the comprehensive conversion of the redox couples of Cu^+/Cu^{2+}, Co^{2+}/Co^{3+} and Co^{3+}/Co^{4+} during the redox reactions,[36] and the individual redox reaction can be described as the eq. 8-10.

$$Cu_2O + 2OH^- \leftrightarrow 2CuO + H_2O + 2e^- \quad (8)$$

$$Co_3O_4 + OH^- + 2H_2O \leftrightarrow 3CoOOH + e^- \quad (9)$$

$$CoOOH + OH^- \leftrightarrow CoO_2 + H_2O + e^- \quad (10)$$

The CV performance of $Cu_{0.27}Co_{2.73}O_4/MnO_2$ is investigated within the scan rate from 5 to 50 mVs^{-1} (**Fig. 9**b). The CV curves are slightly different from that of $Cu_{0.27}Co_{2.73}O_4$, which is attributed to the participation of MnO_2 in the pseudocapacitive reaction during the charge storage process that makes contribution to final capacitance. As well known, the charge storage capacity of MnO_2 electrodes in aqueous KOH is based on the following two mechanisms:[37] (i) surface adsorption and desorption of K^+ ions on MnO_2 surface (nonfaradic process, eq.11) and (ii) intercalation/deintercalation of K^+ ions into/from the electrode material accompanied with redox reactions (faradic process, eq.12), respectively.

$$(MnO_2)_{surface} + K^+ + e^- \leftrightarrow (MnO_2K^+)_{surface} \quad (11)$$

$$MnO_2 + K^+ + e^- \leftrightarrow MnO \bullet OK \quad (12)$$

It should be noted that the coated MnO_2 nanoflake layers does not shield the inside $Cu_{0.27}Co_{2.73}O_4$, so the capacitance originates from both $Cu_{0.27}Co_{2.73}O_4$ and MnO_2. It is shown that the integral area of the CV curves increases with the incorporation of MnO_2 nanoflakes on the surface of $Cu_{0.27}Co_{2.73}O_4$ nanorods (**Fig. S3**c, d), suggesting electrochemical activity enhancement due to the coupling $Cu_{0.27}Co_{2.73}O_4$ nanorod arrays with MnO_2 nanoflakes. In pseudocapacitive electrode materials, the correlation between oxidation peak current I and scan rate v is commonly used to determine whether the capacitance originates from electrochemical double layer or redox reaction. The former can give a representative relationship of $i \propto v$ like the ideal parallel plate capacitor, and the latter can follow $i \propto v^{1/2}$, because it is dominated by semi-infinite bulk diffusion process. The plots of peak current i versus $v^{1/2}$ in **Fig. 10** show a well fitted linear relationship between the current density and scan rate for both $Cu_{0.27}Co_{2.73}O_4/MnO_2$ and $Cu_{0.27}Co_{2.73}O_4$ electrodes, clearly demonstrating that bulk diffusion behavior is the main factor to dominate the current density.[18, 23, 38]

To estimate electrochemical capacitance from redox reactions, galvanostatic charge-discharge (GCD) measurement is further performed from -0.05 V to 0.55V. Relying on the GCD profiles in **Fig. 11**a-**11**b and **Fig. S3.**b, we figure out the capacitance through eq. 6 and 7. The capacity (C_a) of $Cu_{0.27}Co_{2.73}O_4$ (**Fig. 11**a) at 2.2, 4.4, 8.8, 13.2, 17.6 $mAcm^{-2}$, are 2.73, 2.68, 2.42, 2.33, 2.24 Fcm^{-2}, while those of $Cu_{0.27}Co_{2.73}O_4/MnO_2$ (**Fig. 11**b) at 3.1, 6.2, 12.4, 18.6 and 24.8 $mAcm^{-2}$ are 3.40, 3.35, 3.27, 3.13 and 3.10 Fcm^{-2}, respectively. The capacitance of Co_3O_4 at different current densities (2.05, 4.1, 8.2, 12.3 and 16.4 $mAcm^{-2}$) is 1.85, 1.80, 1.77, 1.74, 1.67 Fcm^{-2}, much lower than those of $Cu_{0.27}Co_{2.73}O_4$ and $Cu_{0.27}Co_{2.73}O_4/MnO_2$ electrodes. This is because the Cu incorporation into lattice of Co_3O_4 facilitates the surface reaction of $MOH + OH^- \rightarrow MO + H_2O + e^-$ to achieve an improvement of O_2 evolution compared to Co_3O_4, enhancing the charge/discharge rate of the capacitors.[39] In other words, the copper cations that distributing in the crystal lattice partially substitute cobalt cations promote the improvement of electrochemical properties. Obviously, along with the increasing current density, less of stored charge is available due to the lag of ions diffusion, leading to a lower areal capacitance. Nevertheless, probably thanks to the facile ion diffusion within the porous 3D interspace, there was still considerable ~82.1% of C_a retained when current density increases from 2.2 to 17.6 $mAcm^{-2}$ for $Cu_{0.27}Co_{2.73}O_4$, ~91.2% maintained for $Cu_{0.27}Co_{2.73}O_4/MnO_2$ from 3.1 to 24.8 $mAcm^{-2}$, revealing a good rate capability. As expected, sufficiently utilization of the space between the nanorods and the modified MnO_2 nanoflakes further enhances the areal capacitance of $Cu_{0.27}Co_{2.73}O_4/MnO_2$ effectively. This strategy should be impressive and effective for practical applications. In addition, the small drop at the beginning of discharge process indicates the low internal resistance of both electrodes, which may come from the well conductivity of $Cu_{0.27}Co_{2.73}O_4$ nanorods. Compared with some ever reported results, the areal capacitance of $Cu_{0.27}Co_{2.73}O_4$ and $Cu_{0.27}Co_{2.73}O_4/MnO_2$ here are much higher than those with similar designed structures.[3, 9, 19-22] The enhancement of C_a benefits from the novel architecture of the samples, and GCD results are well in agreement with CV curve results.

The long-time cycle performance and durability are of great importance for ECs. **Fig. 12** exhibits the capacity changes during 3000 cycles of galvanostatic charge-discharge (GCD) process for the $Cu_{0.27}Co_{2.73}O_4$ and $Cu_{0.27}Co_{2.73}O_4/MnO_2$. The areal capacitance increases slightly in the beginning 1000 cycles with the cycle number

increasing. This is because the electrolyte gradually penetrates and more active sites are activated.[22] Finally, the capacity stabilize at value of 4 and 2 Fcm^{-2}, respectively. This process is further confirmed by charge-discharge curves in **Fig. S4**, showing the difference between first 10 and last 10 charge-discharge curves during 3000 cycles of $Cu_{0.27}Co_{2.73}O_4$ at 8.8 $mAcm^{-2}$ and $Cu_{0.27}Co_{2.73}O_4/MnO_2$ at 18.6 $mAcm^{-2}$. As we can see, both electrodes exhibit excellent cycling stability within 3000 cycles. The enhancement of the electrochemical properties benefits from the synergistic effect between $Cu_{0.27}Co_{2.73}O_4$ and MnO_2. Similar phenomena are ever reported, for example, the synergistic effect between Co_9S_8 nanorod arrays (with large specific surface and high conductivity) and $Ni(OH)_2$ nanosheets (with excellent electrochemical properties), is used to obtain better rate capability and cycling stability than that of pure Co_9S_8 and $Ni(OH)_2$.[40] It is reported that the urchin-like $NiCo_2(CO_3)_{1.5}(OH)_3$@$NiCo_2S_4$ hybrids on Ni foam display a great enhancement of the electrochemical performances compared with individual $NiCo_2(CO_3)_{1.5}(OH)_3$ or $NiCo_2S_4$ component on Ni foam, which is generally believed to be attributed to the synergistic effect between the two different components with corresponding advantages, in which the core of $NiCo_2(CO_3)_{1.5}(OH)_3$ can exhibit outstanding cycle stability, and the $NiCo_2S_4$ shell can exhibit high electrochemical rate capability.[41] Similarly, The enhanced electrochemical performances of Co_3O_4/SnO_2@MnO_2 should benefit from the synergistic effect between Co_3O_4/SnO_2 nanobox core and MnO_2 nanosheet shell that facilitates diffusion of electrolyte ion diffusion and dispersion of active materials.[42]

As stated above, there are pressing requirements for the electrode materials not only delivering higher areal capacitance, but also providing enough energy in miniaturized devices, which requests the electrode to keep a large areal capacitance at a high current density. Correspondingly, the prepared $Cu_{0.27}Co_{2.73}O_4/MnO_2$ exhibits a superior areal capacitance of 4 Fcm^{-2}, larger than 0.72 Fcm^{-2} of Co_3O_4@MnO_2 core-shell arrays[19] and 2.4 Fcm^{-2} of CoO@NiHON,[20] even at a higher current density of 18.6 mA cm^{-2} than 4 $mAcm^{-2}$ and 5$mAcm^{-2}$ of the latter two works. The superior performance of the $Cu_{0.27}Co_{2.73}O_4/MnO_2$ can be ascribed to the unique 3D hierarchical core/shell structure, which contributes to (i) improve the path way for ion-diffusion and electron-transportation, (ii) high mass loading of ~6.2 mg cm^{-2}, larger than the latter two, and (iii) sufficient utilization of the active materials. In addition, both $Cu_{0.27}Co_{2.73}O_4$ and $Cu_{0.27}Co_{2.73}O_4/MnO_2$ exhibits excellent cycling stability with the coulombic efficiency maintaining ~97% after 3000 cycles.

To gain further insight into the charge transfer behavior related to electrochemical performance, electrochemical impedance spectra (EIS) measurement is carried out at room temperature. Generally speaking, EIS spectra display a similar modality that consists of an arc in higher frequency region and a spike at lower frequency range.[43] Specially, in the equivalent circuit, the equivalent series resistance, R_{ESR} (consisting of ionic resistance of the electrolyte, intrinsic electronic resistance of the electrode material and contact resistance at interfaces) can be determined by the intercept at real part Z' in **Fig. 13**. The charge transfer resistance, R_{CT} (representing Faradaic reaction resistance) and double-layer capacitance, C_{DL} (originating from the formation of the electrical double layer at the electrode/electrolyte interface) correspond to the semicircle in the high-frequency region. The slope of the 45º portion in the mid-frequency range is called Warburg resistance, Z_W (describing the frequency dependence process of the electrolyte ions diffusing into/out of the electrode material). The limit capacitance, C_{LC}, describes the resistance at the very low frequency.[43-46] For comparison, the Co_3O_4 nanorod arrays that synthesized in the same situation are also determined by EIS measurement under the identical condition. The charge saturation point usually to determine the power capability of an electrochemical capacitor in

the Nyquist plots shown by the insert of **Fig. 13** is known as the "knee" frequency (f_{knee}), and the "knee" frequency (f_{knee}) and the f_{knee} of Co_3O_4, $Cu_{0.27}Co_{2.73}O_4$ and $Cu_{0.27}Co_{2.73}O_4$@MnO_2 is 14.2, 17.3 and 27.6 Hz, respectively. As is known, a higher f_{knee} means the faster capacitive response,[47] so $Cu_{0.27}Co_{2.73}O_4/MnO_2$ displays better capacitive response characteristic.

According to the bode-absolute curves in **Fig. 14**, we can get the absolute resistance of the as-synthesized samples. As revealed by EIS result, the R_{ESR} of $Cu_{0.27}Co_{2.73}O_4$ and $Cu_{0.27}Co_{2.73}O_4/MnO_2$ are 0.44 and 0.36 Ω, indicating charge transfer kinetics can be greatly improved through the combination of the $Cu_{0.27}Co_{2.73}O_4$ and MnO_2, showing a synergistic effect between the $Cu_{0.27}Co_{2.73}O_4$ and MnO_2. Both the inter-space between adjacent rods, and the pores between adjacent particles facilitate the effective electrolyte penetration into electrode materials, thus lowering the resistance. However, the R_{ESR} of $Cu_{0.27}Co_{2.73}O_4/MnO_2$ is slightly lower than that of $Cu_{0.27}Co_{2.73}O_4$, and the R_{CT} is slightly higher, lying in the fact that the ultrathin and porous morphology of MnO_2 is easier for electrolyte penetration, but their diffusion distance is longer than that of $Cu_{0.27}Co_{2.73}O_4$.

4. Conclusions

In summary, hierarchical $Cu_{0.27}Co_{2.73}O_4/MnO_2$ nanorod arrays directly grown on pressed nickel foam are successfully synthesized by a simple hydrothermal method. The $Cu_{0.27}Co_{2.73}O_4$ nanorods with planar tips and rough surface exhibit a homogeneously aligned structure and uniformly cover the substrate that are benefit for separating the adjacent nanorods, controlling the aggregation of the active materials and improving the path way for ions diffusion and electron transportation. $Cu_{0.27}Co_{2.73}O_4/MnO_2$ not only maintains all of the structural characteristics of $Cu_{0.27}Co_{2.73}O_4$, but also takes advantages of the ultrathin and nearly transparent MnO_2-nanoflake shells to enhance its electrochemical properties. The advantage of our componential and structural design over the methods such as binder-free materials, conductive surface coating, surface modification, etc. improving the conductivity is the enhancement of mine can extend to most of the sites where redox reaction took place, which is the essential way to improve the electrical conductivity and can be confirmed though the EIS results. It is shown that the $Cu_{0.27}Co_{2.73}O_4/MnO_2$ nanoarrays grown on pressed nickel foam possesses high capacitance, excellent rate capability and stable cycle durability, acting as promising electrode materials for high performance ECs.

Acknowledgements

We acknowledge support from the National Nature Science Foundation of China (No.: 51272137, 51472148), The National Basic Research Program (No: 2013CB934303), and the Tai Shan Scholar Foundation of Shandong Province.

References

1 P. Simon and Y. Gogotsi, *Nat. Mater.*, 2008, **7**, 845-854.

2 Y. Wang and G. Cao, *Adv. Mater.*, 2008, **20**, 2251-2269.

3 L. Shen, Q. Che, H. Li, et al., *Adv. Funct. Mater.*, 2014, **24**, 2630-2637.

4 P. Simon, Y. Gogotsi and B. Dunn, *Science Magazine*, 2014, **343**, 1210-1211.

5 J. R. Miller and P. Simon, *Science Magazine*, 2008, **321**, 651-652.

6 Y. Gogotsi, *ACS nano*, 2014, **8**, 5369-5371.

7 M. Beidaghi and Y. Gogotsi, *Energy & Environ. Sci.*, 2014, **7**, 867.

8 T. Y. Wei, C. H. Chen, H. C. Chien, et al., *Adv. Mater.*, 2010, **22**, 347-351.

9 C. Yuan, L. Yang, L. Hou, et al., *Energy & Environ. Sci.*, 2012, **5**, 7883.

10 H. Jiang, J. Ma and C. Li, *Chem. Commun.*, 2012, **48**, 4465-4467.

11 J. Liang, Z. Fan, S. Chen, et al., *Chem. Mater.*, 2014, **26**, 4354-4360.

12 C. C. Hu, K. H. Chang, M. C. Lin, et al., *Nano Lett.*, 2006, **6**, 2690-2695.

13 L. Yu, G. Zhang, C. Yuan, et al., *Chem. Commun.*, 2013, **49**, 137-139.

14 Z. Lu, Q. Yang, W. Zhu, et al., *Nano Res.*, 2012, **5**, 369-378.

15 C. C. Hu, W. C. Chen and K. H. Chang, *J. Electrochem. Soc.*, 2004, **151**, A281-A290.

16 Y. Gogotsi and P. Simon, *Science Magazine*, 2011, **334**, 917-918.

17 J. Chmiola, C. Largeot, P. L. Taberna, et al., *Science*, 2010, **328**, 480-483.

18 W. Zhu, Z. Lu, G. Zhang, et al., *J. Mater. Chem. A*, 2013, **1**, 8327.

19 J. Liu, J. Jiang, C. Cheng, et al., *Adv. Mater.*, 2011, **23**, 2076-2081.

20 C. Guan, J. Liu, C. Cheng, et al., *Energy & Environ. Sci.*, 2011, **4**, 4496.

21 J. Liu, J. Jiang, M. Bosman, et al., *J. Mater. Chem.*, 2012, **22**, 2419.

22 X. Xia, J. Tu, Y. Zhang, et al., *ACS nano*, 2012, **6**, 5531-5538.

23 C. Yuan, J. Li, L. Hou, et al., *Adv. Funct. Mater.*, 2012, **22**, 4592-4597.

24 K. Qiu, Y. Lu, D. Zhang, et al., *Nano Energy*, 2015, **11**, 687-696.

25 B. Liu, J. Zhang, X. Wang, et al., *Nano Lett.*, 2012, **12**, 3005-3011.

26 Q. Wang, X. Wang, B. Liu, et al., *J. Mater. Chem. A*, 2013, **1**, 2468.

27 A. Pendashteh, M. S. Rahmanifar, R. B. Kaner, et al., *Chem . Commun.*, 2014, **50**, 1972-1975.

28 J. Cheng, H. Yan, Y. Lu, et al., *J. Mater. Chem. A*, 2015, **3**, 9769-9776.

29 X. Zhang, Y. Zhao and C. Xu, *Nanoscale*, 2014, **6**, 3638-3646.

30 Y. Gao, S. Chen, D. Cao, et al., *J. Power Sources*, 2010, **195**, 1757-1760.

31 J. Jiang, J. Liu, X. Huang, et al., *Cryst. Growth & Des.*, 2009, **10**, 70-75.

32 Y. Li, L. Cao, L. Qiao, et al., *J. Mater. Chem. A*, 2014, **2**, 6540-6548.

33 A. Tavares, M. da Silva Pereira, M. Mendonça, et al., *J. Electroanal. Chem.*, 1998, **449**, 91-100.

34 M. De Koninck, S. C. Poirier and B. t. Marsan, *J. Electrochem. Soc.*, 2006, **153**, A2103.

35 J. Gautier, E. Rios, M. Gracia, et al., *Thin Solid Films*, 1997, **311**, 51-57.

36 Y. Lei, Y. Wang, W. Yang, et al., *RSC Adv.*, 2015, **5**, 7575-7583.

37 J. Yan, E. Khoo, A. Sumboja, et al., *ACS nano*, 2010, **4**, 4247-4255.

38 B. Vidyadharan, R. A. Aziz, I. I. Misnon, et al., *J. Power Sources*, 2014, **270**, 526-535.

39 I. Nikolov, R. Darkaoui, E. Zhecheva, et al., *J. Electroanal. Chem.*, 1997, **429**, 157-168.

40. J. Wen, S. Li, B. Li, et al., *J. Power Sources*, 2015, **284**: 279-286.

41. B.Yang, L.Yu, H.Yan, et al., *J. Mater. Chem. A*, **2015**. DOI: 10.1039/C5TA02684A

42. M. Huang, X. L. Zhao, F. Li, et al., *J. Mater. Chem. A*, **2015**. DOI: 10.1039/C5TA02144H

43 Z. Fan, J. Yan, T. Wei, et al., *Adv. Funct. Mater.*, 2011, **21**, 2366-2375.

44 J. Gamby, P. Taberna, P. Simon, et al., *J. Power Sources*, 2001, **101**, 109-116.

45 A. Di Fabio, A. Giorgi, M. Mastragostino, et al., *J. Electrochem. Soc*., 2001, **148**, A845-A850.

46 M. S. Wu, C. Y. Huang and K. H. Lin, *J. Power Sources*, 2009, **186**, 557-564.

47 R. Ding, L. Qi, M. Jia, et al., *J. Appl. Electrochem*., 2012, **42**, 1033-1043.

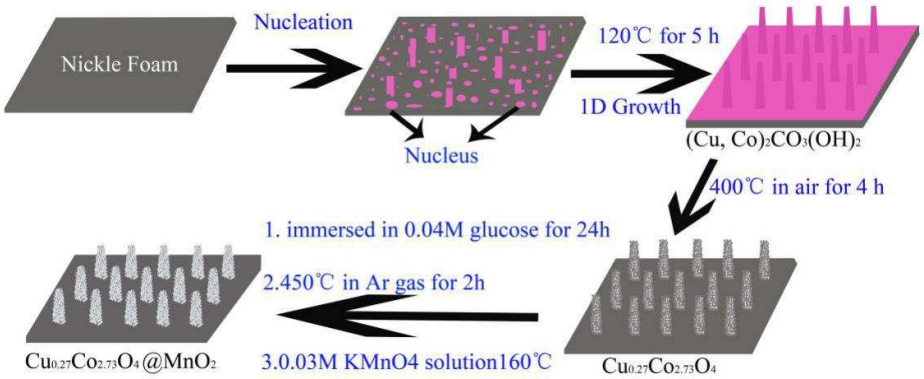

Figure 1. Illustration of the fabrication process of $Cu_{0.27}Co_{2.73}O_4/MnO_2$ hierarchical heterostructures. (a) Nickel foam substrate; (b, c) Hydrothermal synthesis of precursor of $Cu_{0.27}Co_{2.73}O_4$ nanorods array; (d, e) Formation of $Cu_{0.27}Co_{2.73}O_4$ nanorods array and $Cu_{0.27}Co_{2.73}O_4/MnO_2$, respectively.

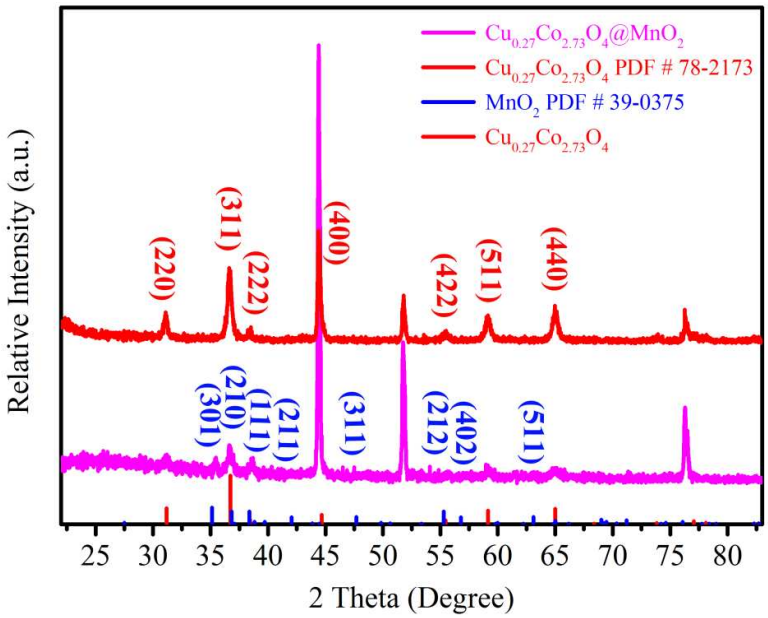

Figure 2. XRD pattern of $Cu_{0.27}Co_{2.73}O_4$ and $Cu_{0.27}Co_{2.73}O_4/MnO_2$ grown directly on nickel foam.

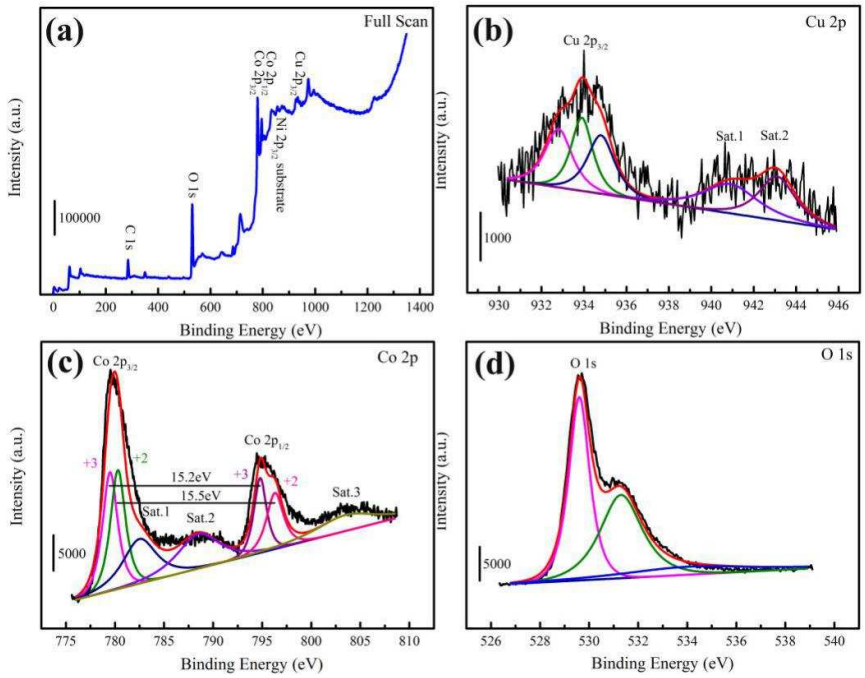

Figure 3. XPS spectrum of $Cu_{0.27}Co_{2.73}O_4$. (a) Full scan, (b) Cu 2p, (c) Co 2p, (d) O 1s.

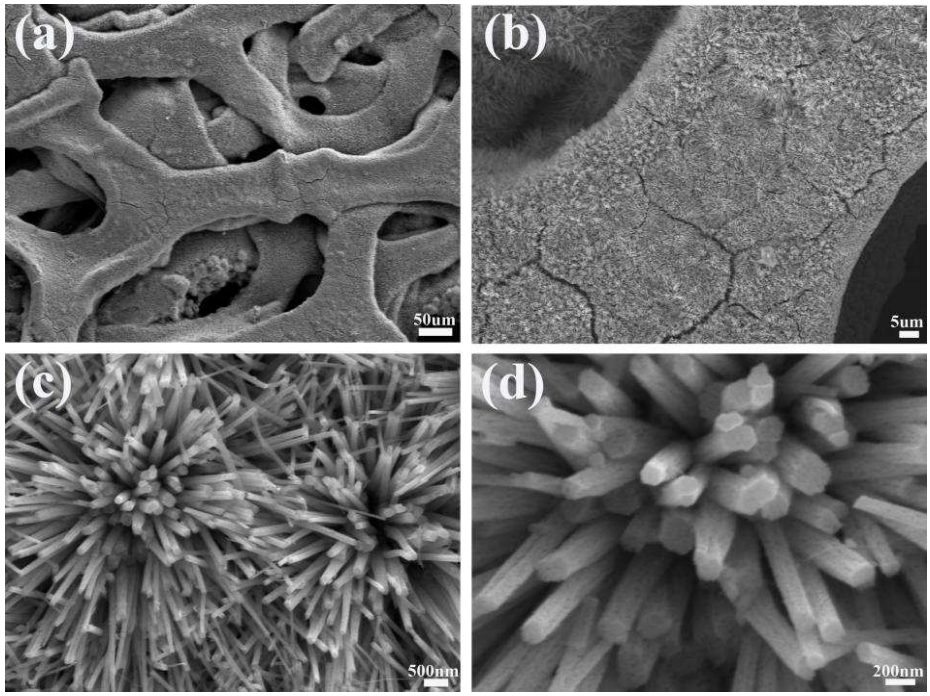

Figure 4. (a-d) SEM images of $Cu_{0.27}Co_{2.73}O_4$ with different magnifications.

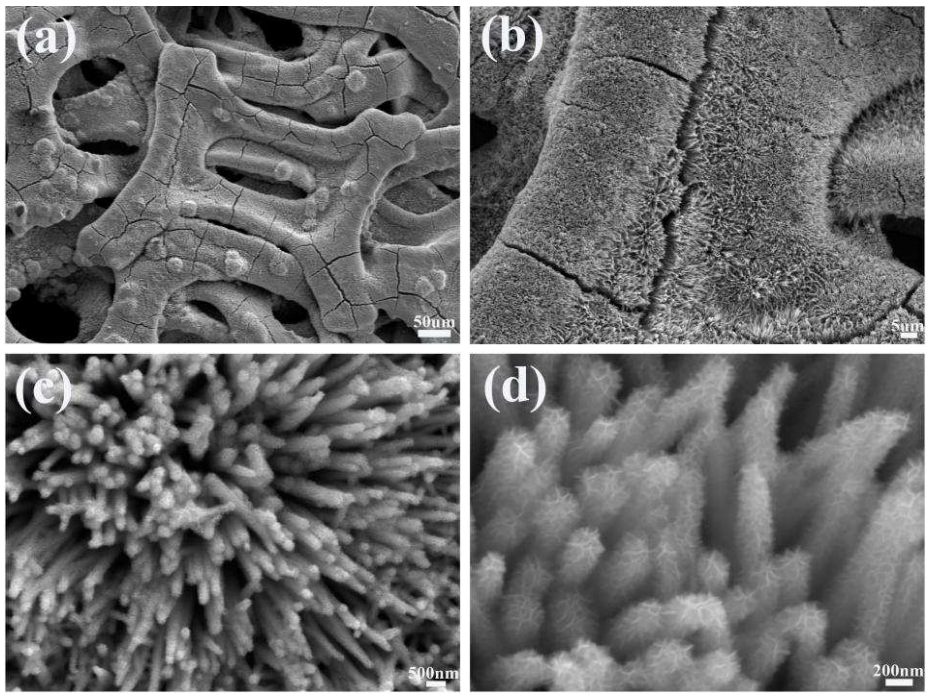

Figure 5. SEM images of $Cu_{0.27}Co_{2.73}O_4/MnO_2$ with different magnifications.

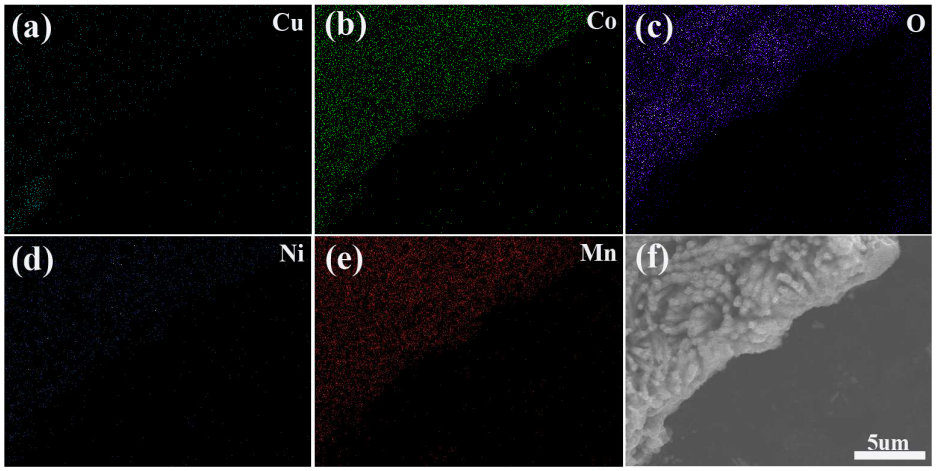

Figure. 6. (a-e) EDS elemental mapping of Cu, Co, O, Ni, Mn elements, suggesting that all the elements are homogeneously distributed among the area in (f).

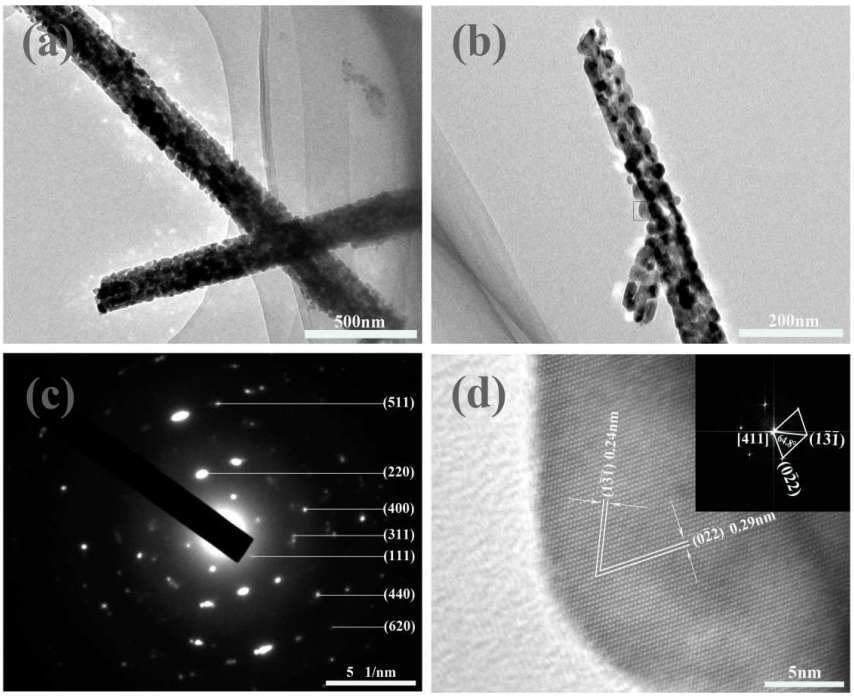

Figure 7. (a-b) TEM images, (c) SAED pattern of $Cu_{0.27}Co_{2.73}O_4$ nanorods, (d) HRTEM image of the grain within gray-boxed area in (b), the insert is the corresponding Fourier transformation pattern.

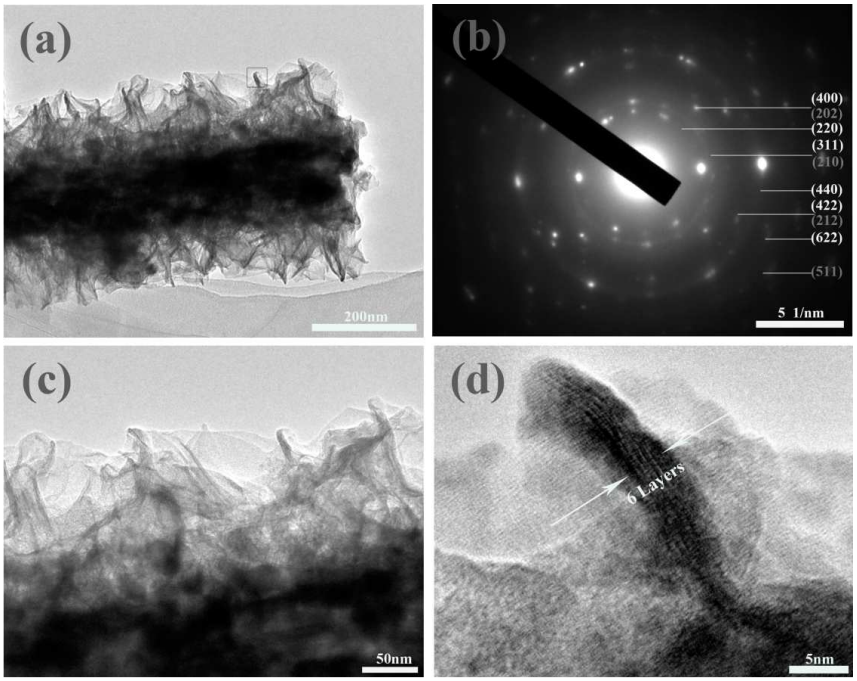

Figure 8. (a) (c) TEM images of with different magnifications, (b) SAED pattern of $Cu_{0.27}Co_{2.73}O_4$@MnO_2, ring markings coloured grayish correspond to that of (210), (202), (212), (511) of MnO_2, the white ones are in agreement with that of (220), (311), (400), (422), (440), (622) of $Cu_{0.27}Co_{2.73}O_4$, (d) Further magnified TEM image of the dark strips within gray-boxed area in (a).

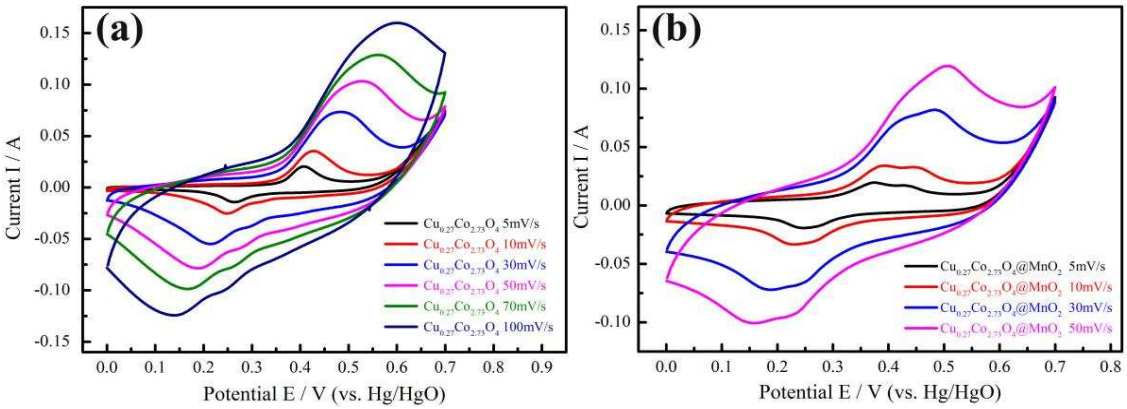

Figure 9. CV curves of (a) $Cu_{0.27}Co_{2.73}O_4$and (b) $Cu_{0.27}Co_{2.73}O_4/MnO_2$ at different scan rates.

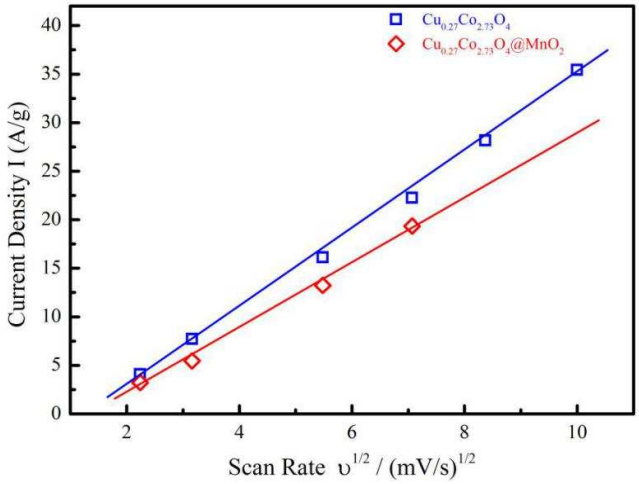

Figure 10. Anodic peak current *I* versus square root of scan rate $\nu^{1/2}$ of $Cu_{0.27}Co_{2.73}O_4$and $Cu_{0.27}Co_{2.73}O_4/MnO_2$, indicating bulk diffusion of ions during the electrochemical reaction.

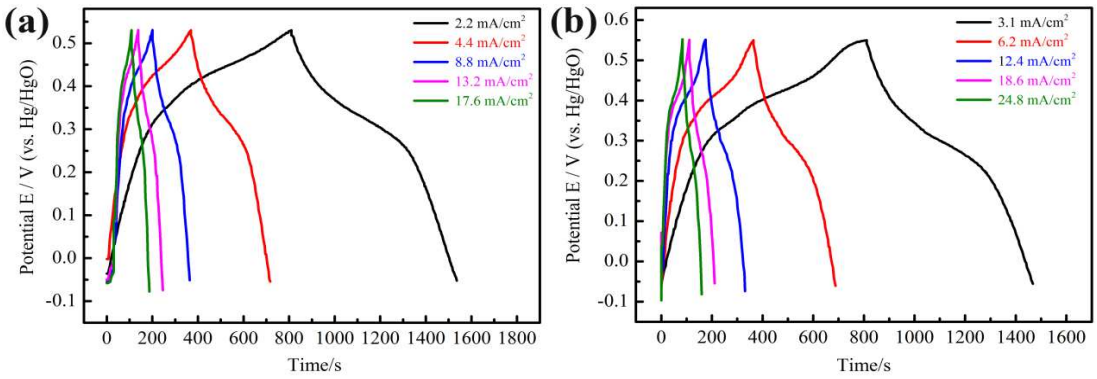

Figure 11. Galvanostatic charge-discharge (GCD) curves of (a) $Cu_{0.27}Co_{2.73}O_4$ and (b) $Cu_{0.27}Co_{2.73}O_4/MnO_2$ at different current densities.

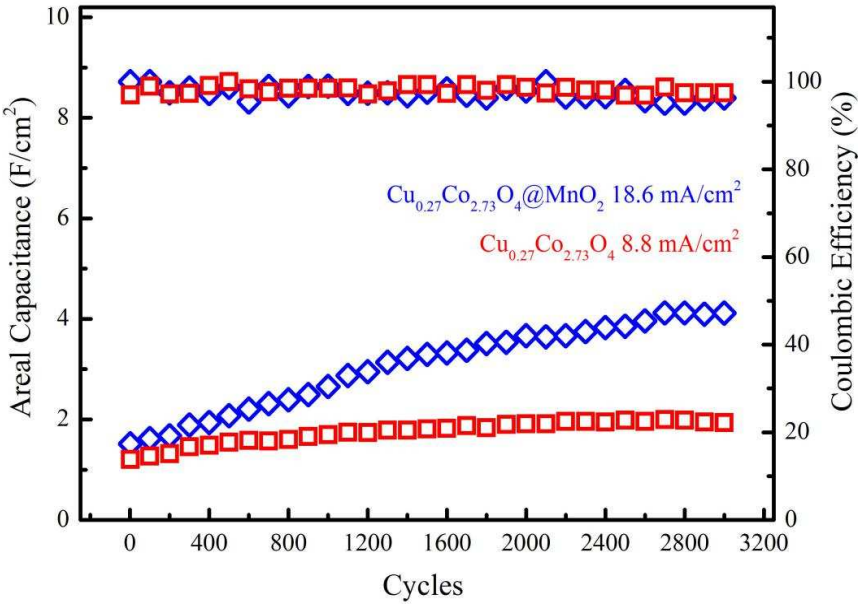

Figure 12. The cycling performance of the $Cu_{0.27}Co_{2.73}O_4$ and $Cu_{0.27}Co_{2.73}O_4/MnO_2$.

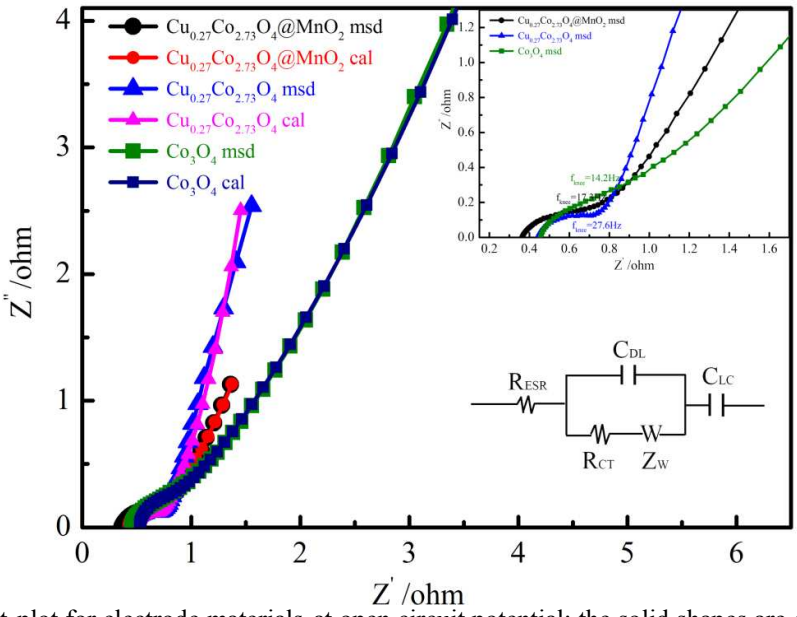

Figure 13. Nyquist plot for electrode materials at open circuit potential; the solid shapes are experimental values and the smaller-sized ones are the fitted data. The insets show the expanded view of experimental ones and the corresponding equivalent circuit.

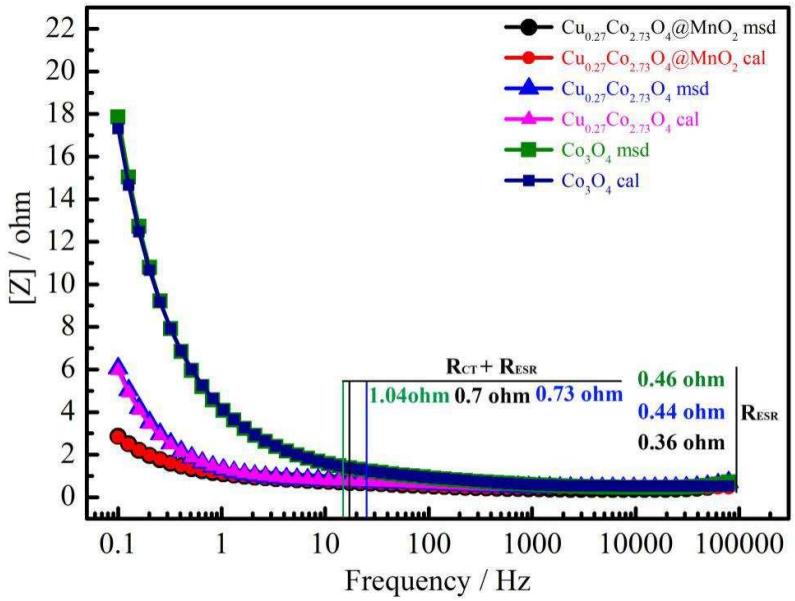

Figure 14. Bode-Absolute curves of the as-synthesized samples, the solid shapes are experimental values and the smaller-sized ones are the fitted data.